

































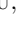




On the Scarcity of Dense Cores ($n > 10^5 \text{ cm}^{-3}$) in High-latitude Planck Galactic Cold Clumps

FENGWEI XU ^{1,2} KE WANG ¹ TIE LIU ³ DAVID EDEN ⁴ XUNCHUAN LIU ³ MIKA JUVELA ⁵ JINHUA HE ^{6,7,8}
DOUG JOHNSTONE ^{9,10} PAUL GOLDSMITH ¹¹ GUIDO GARAY ⁸ YUEFANG WU ^{2,1} ARCHANA SOAM ¹²
ALESSIO TRAFICANTE ¹³ ISABELLE RISTORCELLI ¹⁴ EDITH FALGARONE ¹⁵ HUEI-RU VIVIEN CHEN ¹⁶
NAOMI HIRANO ¹⁷ YASUO DOI ¹⁸ WOJIN KWON ^{19,20} GLENN J. WHITE ^{21,22} ANTHONY WHITWORTH ²³
PATRICIO SANHUEZA ^{24,25} MARK G. RAWLINGS ^{26,27} DANA ALINA ²⁸ ZHIYUAN REN ²⁹ CHANG WON LEE ^{30,31}
KEN'ICHI TATEMATSU ^{32,25} CHUAN-PENG ZHANG ^{33,34} JIANJUN ZHOU ^{35,36,37} SHIH-PING LAI ¹⁷
DEREK WARD-THOMPSON ³⁸ SHENG-YUAN LIU ¹⁷ QILAO GU ³ ESWARIAH CHAKALI ³⁹ LEI ZHU ²⁹
DIEGO MARDONES ⁸ AND L. VIKTOR TÓTH ⁴⁰

¹Kavli Institute for Astronomy and Astrophysics, Peking University, Beijing 100871, People's Republic of China

²Department of Astronomy, School of Physics, Peking University, Beijing, 100871, People's Republic of China

³Shanghai Astronomical Observatory, Chinese Academy of Sciences, 80 Nandan Road, Shanghai 200030, People's Republic of China

⁴Armagh Observatory and Planetarium, College Hill, Armagh, BT61 9DG, UK

⁵Department of Physics, University of Helsinki, PO Box 64, FI-00014 Helsinki, Finland

⁶Yunnan Observatories, Chinese Academy of Sciences, 396 Yangfangwang, Guandu District, Kunming, 650216, People's Republic of China

⁷Chinese Academy of Sciences South America Center for Astronomy, National Astronomical Observatories, CAS, Beijing 100101, People's Republic of China

⁸Departamento de Astronomía, Universidad de Chile, Las Condes, 7591245 Santiago, Chile

⁹NRC Herzberg Astronomy and Astrophysics, 5071 West Saanich Road, Victoria, BC, V9E 2E7, Canada

¹⁰Department of Physics and Astronomy, University of Victoria, 3800 Finnerty Road, Elliot Building, Victoria, BC, V8P 5C2, Canada

¹¹Jet Propulsion Laboratory, California Institute of Technology, Pasadena CA 91109, USA

¹²Indian Institute of Astrophysics, II Block, Koramangala, Bengaluru 560034, India

¹³IAPS-INAF, Via Fosso del Cavaliere, 100, I-00133 Rome, Italy

¹⁴Université de Toulouse, UPS-OMP, IRAP, F-31028 Toulouse cedex 4, France

¹⁵LPENS, Ecole Normale Supérieure, Université PSL, CNRS, Sorbonne Université, Université de Paris, 75005 Paris, France

¹⁶Institute of Astronomy and Department of Physics, National Tsing Hua University, Hsinchu 30013, Taiwan

¹⁷Institute of Astronomy and Astrophysics, Academia Sinica, No.1, Sec. 4, Roosevelt Road, Taipei 10617, Taiwan

¹⁸Department of Earth Science and Astronomy, Graduate School of Arts and Sciences, The University of Tokyo, 3-8-1 Komaba, Meguro, Tokyo 153-8902, Japan

¹⁹Department of Earth Science Education, Seoul National University, 1 Gwanak-ro, Gwanak-gu, Seoul 08826, Republic of Korea

²⁰SNU Astronomy Research Center, Seoul National University, 1 Gwanak-ro, Gwanak-gu, Seoul 08826, Republic of Korea

²¹School of Physical Sciences, The Open University, Walton Hall, Milton Keynes, MK7 6AA, UK

²²RAL Space, STFC Rutherford Appleton Laboratory, Chilton, Didcot, Oxfordshire, OX11 0QX, UK

²³School of Physics and Astronomy, Cardiff University, The Parade, Cardiff, CF24 3AA, UK

²⁴National Astronomical Observatory of Japan, National Institutes of Natural Sciences, 2-21-1 Osawa, Mitaka, Tokyo 181-8588, Japan

²⁵Astronomical Science Program, The Graduate University for Advanced Studies, SOKENDAI, 2-21-1 Osawa, Mitaka, Tokyo 181-8588, Japan

²⁶Gemini Observatory/NSF's NOIRLab, 670 N. A'ohōkū Place, Hilo, HI 96720, USA

²⁷East Asian Observatory, 660 N. A'ohōkū Place, University Park, Hilo, HI 96720, USA

²⁸Nazarbayev University, Kabanbay Batyr Ave, 53, Astana 010000 Kazakhstan

²⁹National Astronomical Observatories, Chinese Academy of Sciences, Datun Rd. A20, Beijing, People's Republic of China

³⁰Korea Astronomy and Space Science Institute, 776 Daedeokdae-ro, Yuseong-gu, Daejeon 34055, Republic of Korea

³¹University of Science and Technology, Korea (UST), 217 Gajeong-ro, Yuseong-gu, Daejeon 34113, Republic of Korea

³²Nobeyama Radio Observatory, National Astronomical Observatory of Japan, National Institutes of Natural Sciences, 462-2 Nobeyama, Minamimaki, Minamisaku, Nagano 384-1305, Japan

³³National Astronomical Observatories, Chinese Academy of Sciences, Beijing 100101, China

³⁴Guizhou Radio Astronomical Observatory, Guizhou University, Guiyang 550000, China

³⁵*XingJiang Astronomical Observatory, Chinese Academy of Sciences, Urumqi 830011, PR China*

³⁶*Key Laboratory of Radio Astronomy, Chinese Academy of Sciences, Urumqi 830011, PR China*

³⁷*Xinjiang Key Laboratory of Radio Astrophysics, Urumqi 830011, PR China*

³⁸*Jeremiah Horrocks Institute, University of Central Lancashire, Preston PR1 2HE, UK*

³⁹*Indian Institute of Science Education and Research (IISER) Tirupati, Rami Reddy Nagar, Karakambadi Road, Mangalam (P.O.), Tirupati 517 507, India*

⁴⁰*Institute of Physics and Astronomy, Eötvös Loránd University, Pázmány Péter sétány 1/A, H-1117 Budapest, Hungary*

ABSTRACT

High-latitude ($|b| > 30^\circ$) molecular clouds have virial parameters that exceed 1, but whether these clouds can form stars has not been studied systematically. Using JCMT SCUBA-2 archival data, we surveyed 70 fields that target high-latitude Planck Galactic cold clumps (HLPCs) to find dense cores with density of 10^5 – 10^6 cm^{-3} and size of < 0.1 pc. The sample benefits from both the representativeness of the parent sample and its coverage of the densest clumps at the high column density end ($> 1 \times 10^{21}$ cm^{-2}). At an average rms of 15 mJy beam^{-1} , we detected Galactic dense cores in only one field, G6.04+36.77 (L183) while also identifying 12 extragalactic objects and two young stellar objects. Compared to the low-latitude clumps, dense cores are scarce in HLPCs. With synthetic observations, the densities of cores are constrained to be $n_c \lesssim 10^5$ cm^{-3} should they exist in HLPCs. Low-latitude clumps, Taurus clumps, and HLPCs form a sequence where a higher virial parameter corresponds to a lower dense-core detection rate. If HLPCs were affected by the Local Bubble, the scarcity should favor turbulence-inhibited rather than supernova-driven star formation. Studies of the formation mechanism of the L183 molecular cloud are warranted.

Keywords: Star formation (1569), Molecular clouds (1072), High latitude field (737)

1. INTRODUCTION

The high latitude (HL) of the Milky Way, also called the “underwater iceberg” guards its secrets about molecular gas and star formation, due in part to the limited scope of previous CO surveys (Xu et al. 2021). Observational challenges essentially originate from the large area of the HL, leading to much longer integration times compared to those required for blind surveys of the Galactic plane. The *Planck* satellite provides an unprecedented all-sky census of the coldest (6–20 K with a median value of ~ 14 K; Planck Collaboration et al. 2011a) Galactic objects by combining the highest-frequency channels of the *Planck* survey 353–857 GHz (i.e., 850–350 μm) with the far-infrared IRAS 100 μm data (Neugebauer et al. 1984; Miville-Deschênes & Lagache 2005). As a result, the *Planck* team has cataloged 13,188 *Planck* Galactic Cold Clumps (PGCCs; Planck Collaboration et al. 2016), including 793 with absolute value of Galactic latitude higher than 30° , a group we refer to as high-latitude Planck cold clumps (HLPCs). Benefiting from the unbiased nature of its parent sample, the 793 HLPCs are the least-biased sample of HL cold dust clumps, therefore serving as a foundation for studying the properties of the HL molecular gas and investigating the initial condition of star formation (Wu et al. 2012; Liu et al. 2013).

Our previous work performed a $^{12}\text{CO}/^{13}\text{CO}/\text{C}^{18}\text{O}$ (1-0) survey toward 41 early cold cores (ECCs; i.e., most reliable detections of PGCCs with signal-to-noise ratio > 15 ; Planck Collaboration et al. 2011b) with the Purple Mountain Observatory (PMO) 13.7 m millimeter-wavelength telescope (Xu et al. 2021). Although detected CO cores have a typical density of several times 10^4 cm^{-3} , consistent with what has been found in nearby molecular cloud cores (Benson & Myers 1983; Myers et al. 1983; Myers & Benson 1983; Myers 1983; Benson & Myers 1989), the turbulent energy is significantly higher than the gravitational energy, with median virial parameters of ~ 35 (Xu et al. 2021). Therefore, our CO surveys unveiled a highly turbulent, diffuse molecular gas environment as a first glimpse of the initial conditions of star formation in the HL clouds.

Stars form in dense cores (Shu et al. 1987) with a typical size of $\lesssim 0.1$ pc and density of 10^5 – 10^6 cm^{-3} (Ward-Thompson et al. 1994, 1999; Kirk et al. 2005). The CO (1-0) transitions suffer from optical thickness and depletion at low temperature, so it is hard to probe the densest regions of molecular clouds. For example, a high-latitude cloud L1780 shows a cometary morphology and a CO core (Toth et al. 1995) but contains no dense core in our survey (field G358.96+36.81). Furthermore, the angular resolution of *Planck* used for the extraction of PGCCs is $\sim 5'$, corresponding to 0.3 pc at a typical

distance of HL clouds of 200 pc (Xu et al. 2021), which is marginal for resolving dense cores. Working at $850\ \mu\text{m}$ with an effective beam FWHM of $14''.6$, Submillimetre Common-User Bolometer Array 2 (SCUBA-2; Dempsey et al. 2013) provides ~ 20 times better resolution than the *Planck*, pinpointing cold dense cores inside the molecular clouds.

In this Letter, we perform a systematic search for dense cores within 70 H LPCs using the latest JCMT SCUBA-2 archival data. The sample selection and distance estimation are summarized in Section 2. As shown in Section 3, dense cores are only identified in one H LPC (G6.04+36.77). In Section 4, we show the robustness of the scarcity of Galactic dense cores in H LPCs, investigate the upper limit of the dense core density, and then discuss star formation picture at high latitude. Finally, we give a brief summary in Section 5.

2. DATA

2.1. Sample Selection

A thorough search of the SCUBA-2 $850\ \mu\text{m}$ data in the JCMT Science Archive¹, and crossmatching with 793 H LPCs that satisfy the latitude criterion of $|b| > 30^\circ$, gave 138 observing fields in total. We dismiss six of the fields that have limited integration time or nonstandard scan modes. Different scan patterns include constant velocity daisy patterns (CV Daisy) and rotating curvy pong patterns (Curvy Pong), so the field offsets vary significantly between different patterns. We make sure that the observing fields cover the peak of PGCCs at 353 GHz. We also check superposition or repetition: if two fields cover the same PGCC, we choose the one with the higher sensitivity. After the work flow, a total of 70 SCUBA-2 fields are selected as the sample in this work.

2.2. Sample Properties

Seventy H LPCs are shown with green crosses, overlaid on the background *Planck* 353 GHz ($850\ \mu\text{m}$) continuum emission in Figure 1. White rectangles outline the CO emission regions defined by Dame et al. (1987). The clump-averaged N_{H_2} H_2 column density N_{H_2} was calculated assuming a dust-emissivity model at 857 GHz (Planck Collaboration et al. 2016). The N_{H_2} distributions of three samples—all the PGCCs, 793 high-latitude PGCCs, and 70 H LPCs—are plotted as gray, blue and orange histograms in Figure 2, respectively. 70 H LPCs has been evenly sampled in the N_{H_2} space, ensuring a similar distribution with its parent sample, 793 HL PGCCs. More importantly, the studied sample

includes the densest clumps at the high-column-density end ($N_{\text{H}_2} > 2.0 \times 10^{21}\ \text{cm}^{-2}$). Considering that the denser clumps should be more likely to produce dense cores, we have covered the complete H LPCs where dense cores could form.

Three regions with relatively higher column density, namely the Orion Frontier, the MBM 12 Complex, and the L134 Complex, are further zoomed in with subpanels in Figure 1. The H LPCs therein correspond to those at the high-density end as mentioned above. The Orion Frontier contains the dark cloud L1642, which together with the MBM 12 Complex are two famous HL clouds that have confirmed star-forming activity (Malinen et al. 2014). The L134 Complex is another region containing several H LPCs, including the widely studied dark cloud L183 (Lee & Myers 1999; Lee et al. 2001; Juvela et al. 2002; Pagani et al. 2003).

2.3. Distance Estimation

Distance is always a difficult quantity to estimate in astronomy. Previous studies have estimated the distances of HL molecular clouds to be 100 pc from the velocity dispersion and the scale height of an ensemble of clouds (Blitz et al. 1984; Magnani et al. 1985). The star counting confirms that the HL molecular clouds are indeed nearby objects with upper limit ranges from 125 to 275 pc (Magnani & de Vries 1986). Using Strömberg photometry, Franco (1989) derive the distances of several H GaL clouds to be 100–230 pc. Both the small V_{lsr} and the lack of a double-sine wave signature in the distribution on the $l - V_{\text{lsr}}$ (Galactic longitude l) plane demonstrate that HL molecular gas belongs to the local interstellar medium (ISM) and is too close to the Sun for Galactic rotation to modulate the velocities (Magnani et al. 1996).

Recently, the *Gaia* satellite has provided new photometric measurements toward galactic stars (Gaia Collaboration et al. 2016). Together with 2MASS and Pan-STARRS 1 optical and near-infrared photometry, *Gaia* DR2 parallaxes can help to infer distances and reddenings of ~ 800 million stars. These stars trace the reddening on a small patch of the sky, along different lines of sight and different distance intervals, allowing us to build a 3D dust-reddening map (Green et al. 2014, 2019). In a given direction, a jump of dust reddening is expected at a distance where there is a dust clump. Distances are estimated by this method and are listed in column (9) of Table A1, with an average value of 200 ± 60 pc, indicating that H LPCs are mostly local ISM. Adopting Eq. 1 in Xu et al. (2021) and considering that the Sun is 10 pc above the Galactic midplane (Griv et al. 2021), the altitude z from the midplane (in units

¹ <https://www.cadc-ccda.hia-ihp.nrc-cnrc.gc.ca/en/jcmt/>

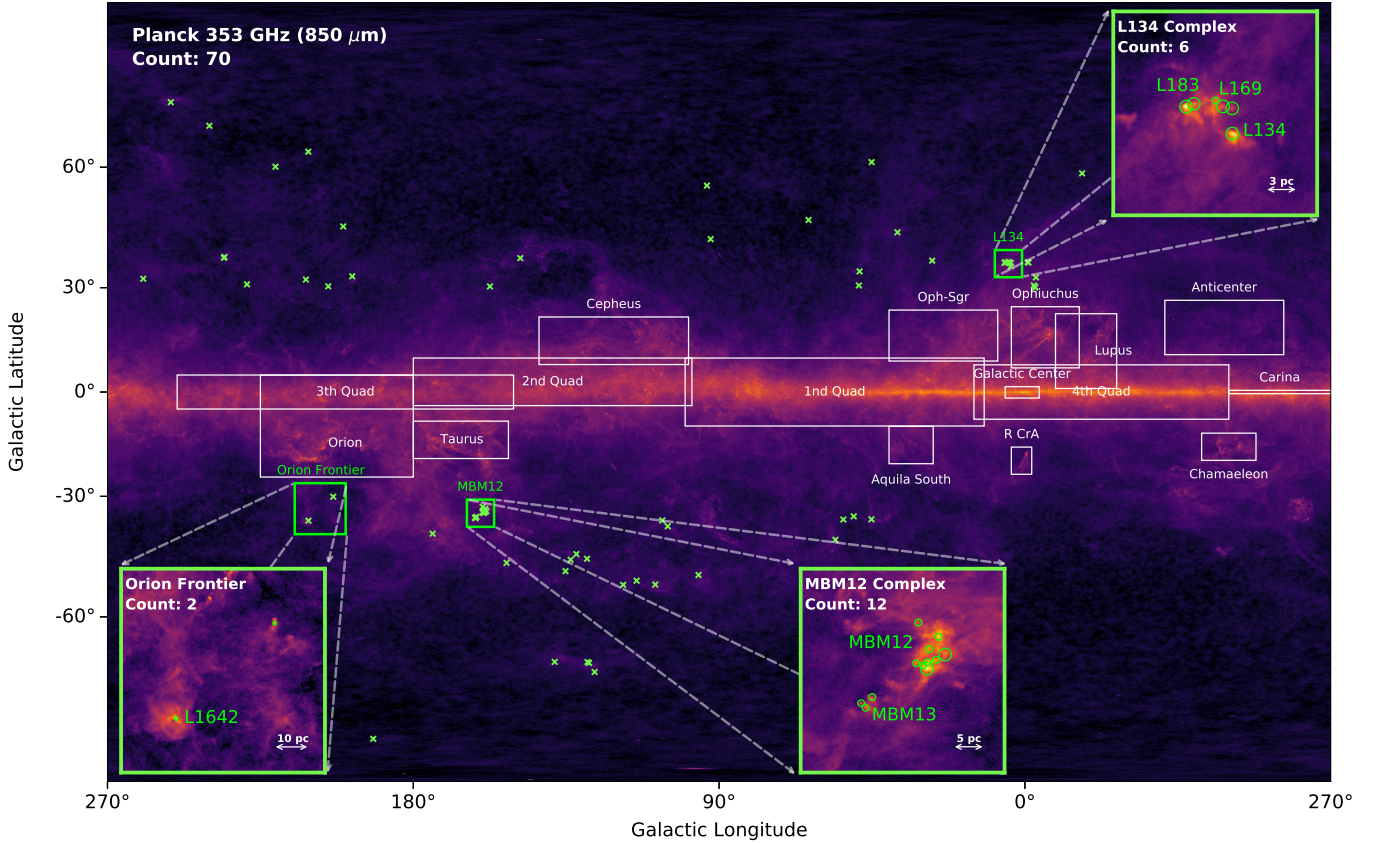


Figure 1. The sky distribution of 70 high-latitude Planck Galactic cold clumps (HLPCs). The background color map is *Planck* 353 GHz ($850 \mu\text{m}$) emission in cylinder projection. The 70 HLPCs are marked with green crosses. Three foreground subregions are zoomed in toward the Orion Frontier, the MBM 12 Complex, and the L134 Complex. The HLPCs in these regions cover the high column density end ($N_{\text{H}_2} > 1.0 \times 10^{21} \text{ cm}^{-2}$). In the zoomed-in subregions, HLPCs are marked with green open circles whose sizes are equivalent to the size of the observing fields. The identifiers in each subregion are marked as green text. The names of the subregions and the number of HLPCs are marked with white text on the upper left. The white rectangles are the CO emission regions.

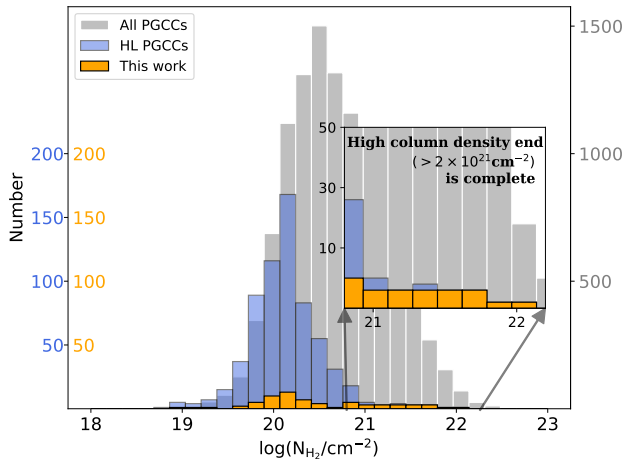


Figure 2. The gray histogram shows the distribution of 13,188 PGCCs. The blue histogram is for 793 high-latitude PGCCs while the orange histogram is for the 70 HLPCs used in this work. A subpanel zooms in the H_2 column density range of $10^{20.8}$ – $10^{22.2} \text{ cm}^{-2}$.

of parsecs) is calculated from $z = d \sin(b) + 10$ where d is the distance and b is the latitude, and listed in column (10). We note that some fields may contain extragalactic objects, so the distance should be only for foreground Galactic dust.

3. RESULTS

3.1. Source Extraction

We adopt the *dendrogram* algorithm (Rosolowsky et al. 2008) to extract dense structures and then measure their integrated flux, peak flux, size, and position by 2D Gaussian fitting. The details of the algorithm parameter settings and the source extraction procedure are introduced in Appendix B. Within the 70 input fields, we have initially detected a total of 20 sources that belong to 15 SCUBA-2 observing fields. The field names and extracted sources are listed in columns (1)–(2) of Table 1. Central coordinates, standard deviation

of the deconvolved major and minor axes, integrated flux, and peak intensity are listed in columns (3)–(7).

3.2. Source Identification and Dense Core Definition

The CV Daisy mode of observation can produce artifacts (Liu et al. 2018; Eden et al. 2019) that are extracted by the algorithm as false source detections. Therefore, we additionally require that both the peak intensity after being smoothed to the *Planck* beam and the total flux of the source at 353 GHz, are lower than those of the parent PGCC. This results in two sources, G50.41-35.40 SMM1 and G197.98+33.10 SMM1, being classified as artifacts and excluded from further analyses. We note that the flux given by the PGCC catalog should be from the cold residual map (Planck Collaboration et al. 2016), so the original *Planck* flux at 353 GHz could be even larger. However, considering the cold nature of dense cores, this should contribute little to the warm component.

We crossmatch the true detections within $1'$ using SIMBAD². We find that only one field, G6.04+36.77, pointing toward the molecular cloud L183, contains three resolved (or marginally resolved) sources, which were previously identified as low-mass prestellar cores (Dickens et al. 2000; Pagani et al. 2003). Our other detections are unresolved as point sources, classified as either young stellar object (YSO) or extragalactic object (point sources) – including gravitational lensed galaxy (LeG), BL Lacertae object (BLL), protocluster of galaxies (PCIG), active nuclei candidate (AGN), and quasar (QSO). The determined identifiers and references are given in columns (8) and (9) of Table 1.

The physical parameters of the L183 dense cores are calculated in Appendix C. Throughout the paper, we adopt the empirical definition of dense core with typical size of $\lesssim 0.1$ pc and density of 10^5 – 10^6 cm^{-3} (Ward-Thompson et al. 1994, 1999; Kirk et al. 2005).

4. DISCUSSION

4.1. Dense Cores Are Scarce In HLPCs

Having only one detection among the 70 HLPCs highlights the scarcity of dense cores at these latitudes. To further confirm this discrepancy compared to the low-latitude ($|b| < 30^\circ$) counterpart, 1235 observing fields from the JCMT Large Project “SCUBA-2 Continuum Observations of Pre-protostellar Evolution” (SCOPE; Liu et al. 2018; Eden et al. 2019) are used as a comparison group because of the following two reasons: (1) twenty-one HLPC fields in this work come from the

SCOPE project so that they have been observed with comparable sensitivities; (2) the SCOPE observations serve as a representative sample of PGCCs, with similar distributions in distance, size, and temperature, and with complete column density coverage over 10^{21} cm^{-2} (Liu et al. 2018).

Considering the beam dilution effects for marginally resolved sources, the column densities are corrected by a beam filling factor $B_{\text{ff}} = (\theta_i^2)/\theta_{\text{PSF}}^2$ where $\theta_{\text{PSF}} = 4.3$ is the *Planck* beam size at 857 GHz (Planck Collaboration et al. 2016) and θ_i is the intrinsic size deconvolved from the beam. For extended sources of which intrinsic size exceeds the beam size, B_{ff} is set to 1, and no correction is performed. As a result, the corrected column density N'_{H_2} increases by a factor of 1.1 on average and 9 at maximum.

In Figure 3, we present the number distributions of different samples across a set of N'_{H_2} bins, denoted as $S_{\text{samp},i}$ where i indicates bin index. Specifically, the distributions for the low-latitude SCOPE fields and the HLPC fields are depicted using the gray and blue histograms, respectively. We also collect the number distribution of those fields with dense cores detected $\{S_{\text{det},i}\}$. The dense core detection rate (DCDR), defined as $\{S_{\text{det},i}/S_{\text{samp},i}\}$, is shown with connected data points. For the low-latitude SCOPE, the DCDR experiences a pronounced increase at a threshold of column density around $N_{\text{H}_2} \simeq 1.0 \times 10^{21}$ cm^{-2} , reaching 90% at the $N_{\text{H}_2} \simeq 5.0 \times 10^{21}$ cm^{-2} regime. The column density threshold for forming dense cores is consistent with what has been found in Gould Belt clouds (e.g., Johnstone et al. 2004). The sudden peak at 3×10^{20} cm^{-2} likely results from the limited sample size. In contrast to the DCDR of the low-latitude SCOPE clumps, the DCDR for the HLPCs remains zero for $N_{\text{H}_2} < 1.0 \times 10^{22}$ cm^{-2} , until dense cores in the HLPC G6.04+36.77 are detected.

The SCOPE serve as a gauge to tell whether the HLPCs have significantly scarce dense cores. Given the null hypothesis that the HLPCs share a DCDR greater or equal to that of the SCOPE, the number of the HLPC fields containing dense cores in each bin of $N_{\text{H}_2} \geq 10^{21}$ cm^{-2} can be predicted, as $\{S_{\text{pred},i}\}_{\text{HLPC}}$. The one-sided Mann–Whitney U test (Mann & Whitney 1947) is performed between the $\{S_{\text{pred},i}\}_{\text{HLPC}}$ and $\{S_{\text{det},i}\}_{\text{HLPC}}$, giving a p-value of 4.8×10^{-3} . This is $\ll 0.05$, thus robustly excluding the null hypothesis. In other words, dense cores are scarce in HLPCs compared to the low latitude.

² <http://simbad.u-strasbg.fr/simbad/>

4.2. What Does “Dense” Mean?

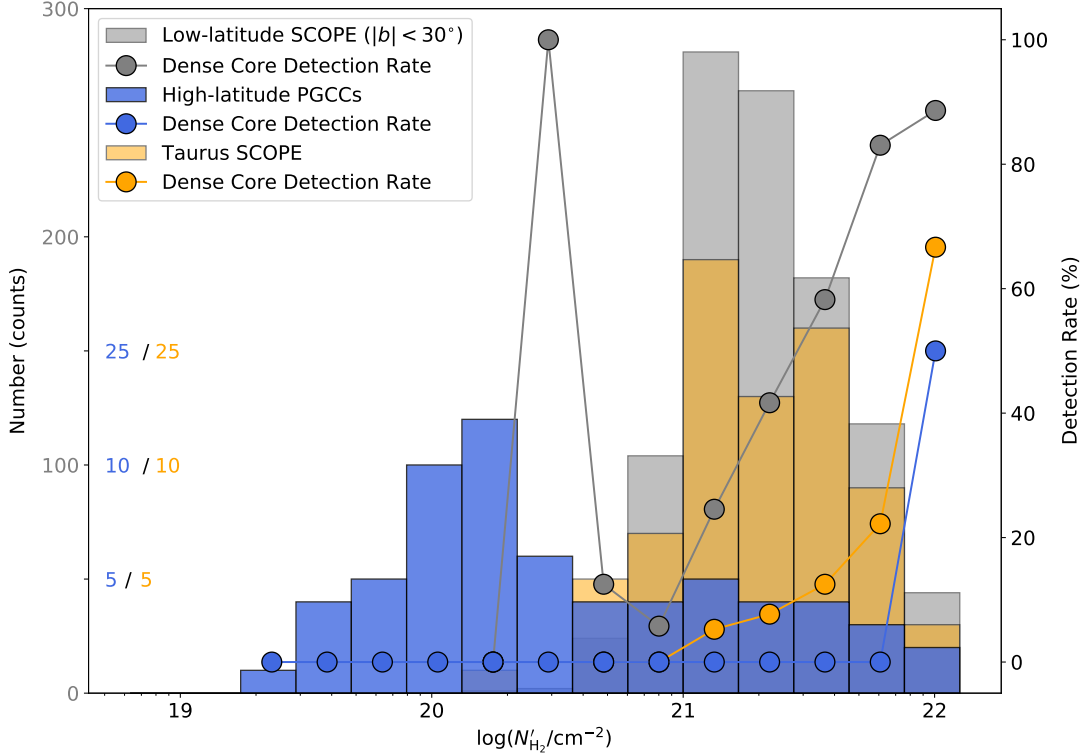


Figure 3. The distribution of column density corrected by beam filling factor N'_{H_2}

for low-latitude SCOPE fields (gray), the HLPC fields (blue) and Taurus SCOPE fields (orange), respectively. The connected data points in corresponding colors depict the DCDR in various N_{H_2} bins.

The scarcity of detection does not necessarily indicate the scarcity of dense cores, primarily due to two factors: (1) the limited sensitivity of identifying sources and (2) the absence of large-scale flux in the SCUBA-2 data processing. Therefore, to understand what the scarcity of dense cores means, it is essential to clarify what “dense” means.

Prestellar cores are observed to have flat inner-density gradients that approach $\rho \sim r^{-2}$ beyond a few thousand astronomical units (Ward-Thompson et al. 1994, 1999; Kirk et al. 2005), which can be reproduced by a nonmagnetic and Plummer-like model (Whitworth & Ward-Thompson 2001) as

$$n_{\text{H}_2}(r) = \frac{n_c}{1 + (r/R_{\text{flat}})^2}, \quad (1)$$

where n_c is the central H_2 number density and R_{flat} is the flat inner radius. The column density profile of such a model core has the analytical form of

$$N_{\text{H}_2}(p) = \frac{2n_c R_{\text{flat}}}{(1 + p^2/R_{\text{flat}}^2)^{1/2}} \times \tan^{-1} \left[\frac{(R_{\text{out}}^2 - p^2)^{1/2}}{(R_{\text{flat}}^2 + p^2)^{1/2}} \right], \quad (2)$$

where p is the distance from core center in the plane of the sky (Dapp & Basu 2009) and $R_{\text{out}} = 0.2 \text{ pc} \simeq 40000 \text{ au}$ defines the boundary of core.

Using the combined ammonia data from the Green Bank Telescope and Karl G. Jansky Very Large Array, the temperatures of the three prestellar cores are observed to have a minor decrease toward the center of the core $\lesssim 2000 \text{ au}$ (Lin et al. 2023). Therefore, we consider a constant temperature profile as $T(r) = T_0 = 10 \text{ K}$ in the following discussion.

Assuming optically thin dust emission, the column density can be used to synthesize model intensity as,

$$I_\nu(p) = \frac{N_{\text{H}_2}(p)\Omega\mu_{\text{H}_2}m_{\text{H}}\kappa_\nu B_\nu(T_{\text{dust}})}{\mathcal{R}}, \quad (3)$$

where $\Omega = \pi\theta_{\text{beam}}^2/4 \ln 2$ measures the solid angle (in unit of radian) per JCMT beam (with FWHM of θ_{beam}), $\mu_{\text{H}_2} = 2.81$ is the molecular weight per hydrogen molecule (Evans et al. 2022), m_{H} is the mass of a hydrogen atom, $\kappa_\nu = 1.22 \text{ cm}^2 \text{ g}^{-1}$ (Beckwith et al. 1990) is the dust opacity at frequency of $\nu = 350 \text{ GHz}$ ($\sim 850 \mu\text{m}$), $B_\nu(T_{\text{dust}})$ is the Planck function at a given dust temperature T_{dust} , and $\mathcal{R} = 100$ is the gas-to-dust mass ratio.

Now we synthesize the SCUBA-2 image $\tilde{I}_\nu(x, y)$ by adding a high-frequency filter $\sqrt{u^2 + v^2} > \xi$, where ξ corresponds to $200''$ in the frequency space (Mairs et al.

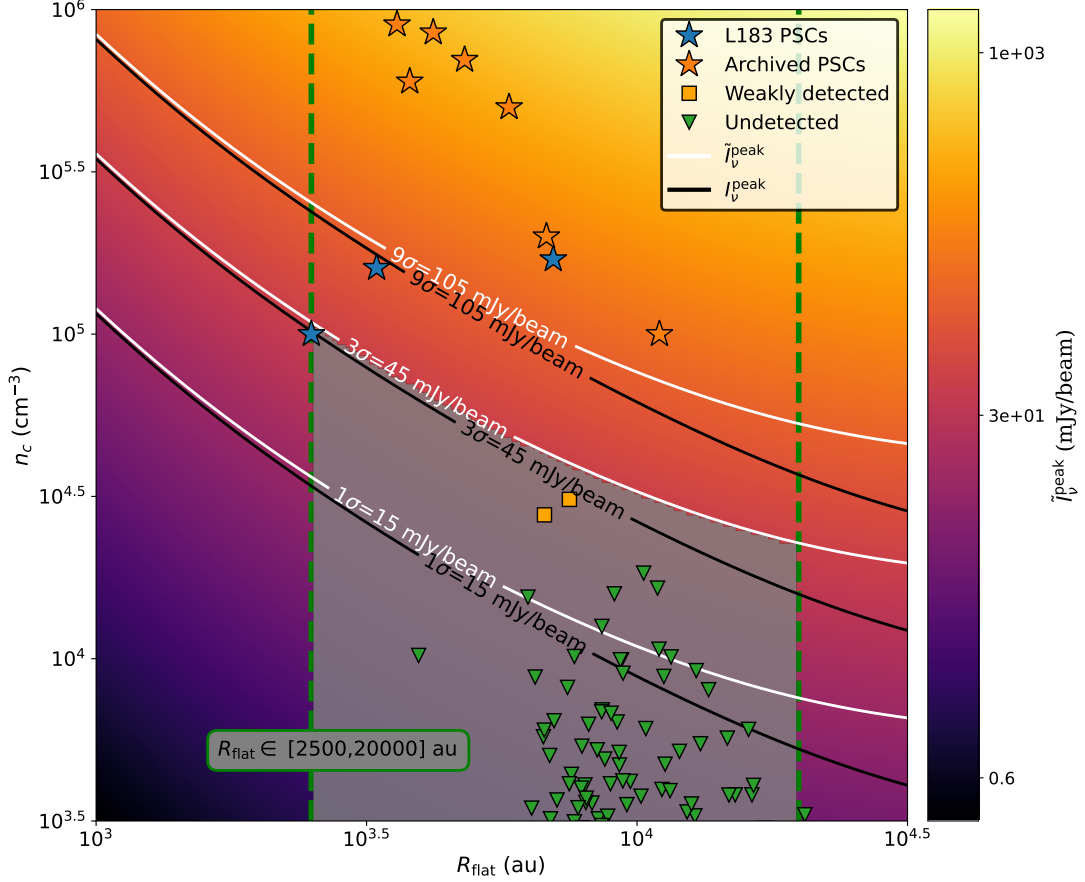


Figure 4. The peak intensity $\tilde{I}_\nu^{\text{peak}}$ observed by SCUBA-2 across parameter space defined by the flat radius $R_{\text{flat}} \in [10^3, 10^{4.5}]$ au and the central density $n_c \in [10^{3.5}, 10^6] \text{ cm}^{-3}$. The white curves mark 1σ , 3σ , and 9σ levels, while the black curves trace the same loci of synthetic model (no large-scale flux filtered out). The green dashed lines delineate the flat inner radius limits $R_{\text{flat}} \in [2500, 20000]$. The shaded gray region indicates the permissible parameter interval of undetected prestellar cores should they exist. Blue and red stars show the L183 prestellar cores and other previously detected prestellar cores (Ward-Thompson et al. 1994, 1999; Kirk et al. 2005). The orange rectangles show two weakly detected cores in our fields. The green triangles show cores detected by Herschel in several HLPCs (Montillaud et al. 2015), but undetected by SCUBA-2.

2015),

$$\tilde{I}_\nu(x, y) = \iint_{\{\sqrt{u^2+v^2} > \xi\}} J_\nu(u, v) e^{i2\pi(ux+vy)} du dv, \quad (4)$$

where $J_\nu(u, v) = \iint I_\nu(x, y) e^{-i2\pi(ux+vy)} dx dy$ is the synthetic model in the Fourier frequency space. As a result, the synthetic observed intensity $\tilde{I}_\nu(x, y)$ can simulate the observed large-scale missing flux at the SCUBA-2 data processing.

In Figure 4, the background color map shows observed peak intensities $\tilde{I}_\nu^{\text{peak}} = \tilde{I}_\nu(0, 0)$ across the 2D parameter space of flat radius $R_{\text{flat}} \in [10^3, 10^{4.5}]$ au and central density $n_c \in [10^{3.5}, 10^6] \text{ cm}^{-3}$. The prestellar cores have been reported to have $R_{\text{flat}} > 2500$ au (Ward-Thompson et al. 1999; Kirk et al. 2005), which are delineated by the left green dashed line in Figure 4. The right green dashed line marks 20,000 au, which corresponds to 0.1 pc.

Consistent with the criteria in the source extraction algorithm (see Appendix B), a threshold of 3σ is adopted to constrain the upper limit of $\tilde{I}_\nu^{\text{peak}}$. As a result, the gray shaded region traces the permissible parameter interval for an undetected core in our observations. In other words, if such cores exist, they should have $n_c < 10^5 \text{ cm}^{-3}$, which is considerably less dense than those that have been identified in nearby low-mass cloud cores (Ward-Thompson et al. 1999; Kirk et al. 2005).

To further demonstrate this upper limit of density, we smooth the images to a resolution of $20''$. With better sensitivity, two new cores (on in HLPC G159.41-34.37 and one in G161.87-35.76) are identified by the same algorithm and parameter input, which are called weakly detected cores. They have radii of about 6700 and 7500 au and averaged density of $2.8 \times 10^4 \text{ cm}^{-3}$ and $3.1 \times 10^4 \text{ cm}^{-3}$, respectively. The two cores are labeled as orange rectangles in Figure 4. We also re-

trieve *Herschel* cold cores in L134 (HLPCs G4.13+35.75 and G4.17+36.67 in our survey), MBM12 (G159.21-34.28, G158.51-33.99, G159.14-33.79, G159.23-34.51, G159.41-34.37, G159.66-34.31), L1642 (G210.90-36.55), and LDN1780 (G358.96+36.81, G359.21+36.89) from [Montillaud et al. \(2015\)](#) which are labeled as green triangles. As they all lie in the gray region which is below the sensitivity limit, these cold cores are not dense enough for detection and are consistently below the density limit of 10^5 cm^{-3} . As noted by [Ward-Thompson et al. \(2016\)](#), SCUBA-2 selects the densest cores from a population at a given temperature, which makes SCUBA-2 ideal for identifying those cores in *Herschel* catalogs that are closest to forming stars. So it is of great interest to study how these low-density cores form and whether they can still form stars or are transient objects.

As indicated by the black curves, peak intensity of a synthetic model I_ν^{peak} is always below the corresponding $\bar{I}_\nu^{\text{peak}}$ outlined by white curves. The difference reflects the missing large-scale flux, which increases in importance from 0.06 to 0.31 dex with R_{flat} from 2500 to 20,000 au. Therefore, if we do not consider missing flux, the density limit can be even lower, especially for those cores with larger flat radius.

4.3. Star Formation at High Galactic Latitude

Low density and high virial parameter lead to a challenge for direct gravitational collapse and then star formation of HL clouds. Observationally, it is consistent with infrared cirrus which is thought to be hostile to star formation ([Low et al. 1984](#)) and the dispersed populations of pre-main-sequence stars (see review by [McGehee 2008](#)). Recently, a clear decreasing trend of N_2H^+ (1-0) and C_2H (1-0) detection rates with latitude is found by [Xu et al. \(2021\)](#). Besides, HCN (1-0) and HCO^+ (1-0) line survey by [Braine et al. \(2023\)](#) reveals that HL molecular clouds have lower dense gas fractions compared to those in the Galactic plane. Theoretically, based on Jeans mass arguments, these low-density turbulent clouds have molecular gas mass lower than the turbulent Jeans mass (see Table 5 in [Xu et al. 2021](#)), therefore unable to fragment into dense dust cores, or protostellar embryos, which agrees with the scarcity of dense cores observed by SCUBA-2.

Previous studies have reported that the virial parameters of the PGCCs in the Taurus region (Taurus clumps hereafter) are predominantly greater than 1, with a median value of approximately 9 ([Meng et al. 2013](#)). This value is considerably lower than the median virial parameter of HLPCs, which stands at about 35. The Taurus clumps covered by the SCOPE project are

designated as the Taurus SCOPE subsample. Figure 3 displays the number distribution and the DCDR for the Taurus SCOPE in orange. In the same way as above, the Mann-Whitney U test gives a p -value of $0.042 < 0.05$, thus favoring that the DCDR of the Taurus clumps is statistically larger than that of HLPCs. Interestingly, the Taurus clumps also exhibit a significantly smaller DCDR compared to the low-latitude SCOPE clumps, as evidenced by a Mann-Whitney U test p -value of 5.4×10^{-3} . This indicates that dense cores within the Taurus clumps are relatively rarer compared to other SCOPE clumps. Consequently, the Taurus clumps occupy an intermediate position between the HLPCs and low-latitude SCOPE clumps in terms of DCDR and virial parameter. The observed trend of decreasing DCDR with increasing virial parameter further substantiates the link between core formation efficiency and the dynamic state of the gas, as previously suggested ([Eden et al. 2019](#)).

HLPCs have a distance of 200 pc which is highly consistent with the radius of the Local Bubble (LB) created by supernovae ([Zucker et al. 2022](#)). The LB is reported to expand and sweep up the ambient interstellar medium into a shell that has now fragmented and collapsed into the most prominent nearby molecular clouds. Interestingly, [Zucker et al. \(2022\)](#) also found that the Taurus star formation region is very likely being compressed by two super bubbles: the local super bubble and the smaller Per-Tau super bubble. If so, it is probable that the formation of dense cores can be hindered by supernova shocks in the solar neighborhood. If the HLPCs and the Taurus clumps were on the shell of LB, the scarcity of dense cores should favor turbulence-inhibited rather than supernova-driven star formation.

On the other hand, the scarcity itself is what gives the only detection (L183) in our survey, as well as a few other clouds (such as MBM 12 and 20), unique status. The capacity of these high-latitude clouds to form cold molecular cores and young stars could arise from a confluence of conditions including variations in the interstellar radiation field, changes in dust grain size and chemistry, the occurrence of shocks, and transient events in the ISM ([McGehee 2008](#)). Consequently, in-depth explorations of the physical and chemical processes within these high-latitude dense cores, for example the L183 dense cores, are merited.

5. CONCLUSION

We performed a JCMT SCUBA-2 archival investigation of 70 fields toward HLPCs to search for dense cores. The sample benefits from being representative of the total HLPC population at low column density

($< 2 \times 10^{21} \text{ cm}^{-2}$) and covering the densest clumps at the high column density end ($> 1 \times 10^{21} \text{ cm}^{-2}$). Using dust reddening in 3D map, the distances of the HLPCs are estimated to be 110–410 pc with a mean value of $200(\pm 60)$ pc. A total of 17 SCUBA-2 sources are identified from a mean noise rms of 15 mJy beam^{-1} . Only one field G6.04+36.77 (L183) contains three dense Galactic cores. The other 14 unresolved sources include 12 extragalactic objects and two Galactic YSOs.

Compared to the low-latitude SCOPE clumps and the Taurus clumps (at a similar distance to HLPCs), the DCDR of HLPCs is significantly lower at the high column density end ($> 1 \times 10^{21} \text{ cm}^{-2}$). Statistical tests verify the scarcity of dense cores in HLPCs. With synthetic observations of known dense cores, the central density of any undetected dense cores is constrained to be $n_c \lesssim 10^5 \text{ cm}^{-3}$, should they exist in HLPCs. The observed scarcity of dense cores aligns with the low-density turbulent environment in HLPCs, as proposed in previous far-infrared and CO line surveys. If the HLPCs and the Taurus clumps were on the shell of the Local Bubble, the scarcity of dense cores should favor turbulence-inhibited rather than supernova-driven star formation. Furthermore, the scarcity also calls for further study on the formation mechanism of L183 dense cores.

ACKNOWLEDGMENT

This work has been supported by the National Key R&D Program of China (No. 2022YFA1603102, 2019YFA0405100), the National Science Foundation of China (12033005, 11973013), and the China Manned Space Project (CMS-CSST-2021-A09, CMS-CSST-2021-B06), and the China-Chile Joint Research Fund (CCJRF No. 2211). CCJRF is provided by Chinese Academy of Sciences South America Center for Astronomy (CASSACA) and established by National Astronomical Observatories, Chinese Academy of Sciences (NAOC) and Chilean Astronomy Society (SOCHIAS) to support China-Chile collaborations in astronomy. T.L. acknowledges the support by the international partnership program of Chinese academy of sciences through grant No.114231KY5B20200009, and Shanghai Pujiang Program 20PJ1415500. This research was carried out in part at the Jet Propulsion Laboratory, which is operated by the California Institute of Technology under a contract with the National Aeronautics and Space Administration (80NM0018D0004). This work is sponsored (in part) by the Chinese Academy of Sciences (CAS), through a grant to the CAS South America Center for Astronomy (CASSACA) in Santiago, Chile. D.J. is supported

by NRC Canada and by an NSERC Discovery grant. G.G. acknowledges support from the ANID BASAL project FB210003. E.F. acknowledges support from the European Council, under the European Community’s Seventh framework Programme, through the Advance Grant MIST (FP7/2017-2024, No. 742719). P.S. was partially supported by a Grant-in-Aid for Scientific Research (KAKENHI Number JP22H01271 and JP23H01221) of JSPS. C.W.L. is supported by the Basic Science Research Program through the National Research Foundation of Korea (NRF) funded by the Ministry of Education, Science and Technology (NRF-2019R1A2C1010851), and by the Korea Astronomy and Space Science Institute grant funded by the Korea government (MSIT) (Project No. 2023-1-84000). G.J.W. gratefully acknowledges receipt of an Emeritus Fellowship from The Leverhulme Trust. M.J. acknowledges support from the Research Council of Finland grant 348342. The work of M.G.R. is supported by NOIRLab, which is managed by the Association of Universities for Research in Astronomy (AURA) under a cooperative agreement with the National Science Foundation. N.H. acknowledges support from the Nation Science and Technology Council (NSTC) of Taiwan with grant NSTC 111-2112-M-001-060.SPL acknowledges the Ministry of Science and Technology of Taiwan for grant 112-2112-M-007-011. This research used the facilities of the Canadian Astronomy Data Centre operated by the National Research Council of Canada with the support of the Canadian Space Agency. The James Clerk Maxwell Telescope is operated by the East Asian Observatory on behalf of The National Astronomical Observatory of Japan; Academia Sinica Institute of Astronomy and Astrophysics; the Korea Astronomy and Space Science Institute; the National Astronomical Research Institute of Thailand; Center for Astronomical Mega-Science (as well as the National Key R&D Program of China with No. 2017YFA0402700). Additional funding support is provided by the Science and Technology Facilities Council of the United Kingdom and participating universities and organizations in the United Kingdom and Canada. Additional funds for the construction of SCUBA-2 were provided by the Canada Foundation for Innovation.

Software: Astropy, a community developed core python package for astronomy (Astropy Collaboration et al. 2013, 2018, 2022). Montage, funded by the National Science Foundation under Grant Number ACI-1440620, and previously funded by the National Aeronautics and Space Administration’s Earth Science Technology Office, Computation Technologies Project, under Cooperative

Agreement Number NCC5-626 between NASA and the California Institute of Technology ([Jacob et al. 2010](#); [Berriman & Good 2017](#)).

Table 1. Detected Sources Catalog

Field	Source	RA	DEC	$\sigma_{\text{maj}} \times \sigma_{\text{min}}$	F_{int}	I_{peak}	Identifier ^{[refs]^a}	Class ^b
(1)	(2)	deg	deg	arcsec ²	Jy	mJy beam ⁻¹	(8)	(9)
G6.04+36.77	SMM1	238.5361	-2.8732	34.2×17.2	3.36	218.4	Position C ^[1] Region 3 ^[2]	PSC
	SMM2	238.5025	-2.8786	10.2×7.4	0.13	57.4	Position W ^[1] Region 4 ^[2]	PSC
	SMM3	238.5404	-2.8154	13.5×10.0	0.35	64.2	Position N ^[1] Region 5 ^[2]	PSC
G45.12+61.11	SMM1	225.6511	29.3460	point	0.08	111.2	PLCK G045.1+61.1 ^[3,4]	LeG
G50.41-35.40	SMM1	321.7839	-2.7151	10.3×8.3	0.52	148.5	-	Artifact
G53.44-36.25	SMM1	323.7980	-1.0478	point	0.09	111.8	SMMJ2135-0102 ^[5]	LeG
G92.49+42.88	SMM1	242.3232	60.7542	point	0.08	110.4	PLCK G092.5+42.9 ^[3,4]	LeG
G152.54-47.36	SMM1	32.8050	10.8598	point	0.89	942.0	J021113.1+105134 ^[6]	BLL
G157.44+30.33	SMM1	113.3787	117.2158	point	0.07	74.8	PLCKESZ ^[7]	CIG
G197.98+33.10	SMM1	128.3946	26.1982	36.8×27.7	6.29	176.6	-	Artifact
G200.62+46.09	SMM1	143.0981	27.4163	point	0.06	75.1	PLCK G200.6+46.1 ^[3]	LeG
G204.99+30.38	SMM1	127.6930	19.6131	point	0.014	20.5	Planck18p194-0 ^[8]	PCIG
	SMM2	127.7268	19.6251	point	0.009	15.4	Planck18p194-1 ^[8]	PCIG
	SMM3	127.6705	19.6631	point	0.008	14.2	Planck18p194-3 ^[8]	PCIG
G210.90-36.55	SMM1	68.7600	-14.2287	point	0.05	64.1	GCVS EW Eri ^[9] MJR2015 1752 ^[10]	V* Y*O
	SMM2	68.7080	-14.2195	point	0.08	82.1	HH123 ^[11] MJR2015 1751 ^[10]	HH Y*O
G211.62+32.23	SMM1	131.7098	15.0943	point	0.11	125.8	J084650.1+150547 ^[12]	AGN?
G228.99+30.91	SMM1	137.2924	1.3599	point	0.23	274.9	4C 01.24B ^[13]	QSO
G343.12+58.61	SMM1	212.5190	2.0516	point	0.04	68.4	J141004.6+020306 ^[14]	BLL

NOTE—The HLPC fields are listed in column (1). The extracted sources are named as SMM \mathcal{X} , as listed in column (2). The equatorial coordinates of R.A. and Dec. in Epoch J2000 are listed in columns (3) and (4). The deconvolved standard deviation along the major and minor axis are listed in columns (5), and marked as “point” if the source is unresolved as a point source. The integrated flux and peak intensity are listed in columns (6) and (7). Identifier(s) and classifications retrieved from SIMBAD are listed in columns (8) and (9).

^a [1] Dickens et al. (2000); [2] Karoly et al. (2020); [3] Cañameras et al. (2015); [4] Frye et al. (2019); [5] Swinbank et al. (2010); [6] Healey et al. (2008); [7] Planck Collaboration et al. (2014); [8] MacKenzie et al. (2017); [9] Samus’ et al. (2017); [10] Montillaud et al. (2015); [11] Reipurth & Heathcote (1990); [12] Truebenbach & Darling (2017); [13] Wright et al. (2009); [14] Plotkin et al. (2008);

^b Classification according to references. PSC—prestellar core. LeG—gravitational lensed galaxy. Artifact—probable artifact by JCMT data reduction pipeline. BLL—BL Lacertae object. CIG—cluster of galaxies. PCIG—proto-cluster of galaxies. V*—variable star. Y*O—young stellar object. HH—Herbig-Haro object. AGN?—active galactic nuclei candidate. QSO—Quasar.

APPENDIX

A. SCUBA-2 OBSERVATION ARCHIVE

Table A1 presents the information for JCMT SCUBA-2 observations toward 70 High Latitude Planck Galactic Cold Clumps (HLPCs). We sort the observations by Galactic longitude and number the fields from 1 to 70. The serial number and the name of HLPC are listed in columns (1) and (2). The equatorial coordinates Right Ascension (RA) and Declination (DEC) of the field

center in Epoch J2000 are listed in columns (3) and (4). The project ID and scan pattern of the JCMT SCUBA-2 observation are listed in columns (5) and (6). The angular offset, which is defined by the angular distance from the field center to the center of the corresponding PGCC, is listed in column (7). The rms noise of the field is listed in column (8). As mentioned in Section 2.3, the estimated distances and altitude are listed in columns (9)–(10).

Table A1. Parameters of 70 High-latitude Planck Galactic Cold Clumps

No.	Field	RA	Dec.	Project ID	Scan Pattern ^a	Offset	rms	Distance	Altitude
		deg	deg			arcmin	mJy beam ⁻¹	pc	pc
(1)	(2)	(3)	(4)	(5)	(6)	(7)	(8)	(9)	(10)
1	G4.13+35.75	238.3879	-4.6406	M14AU35	Curvy Pong	2.17	6.2	140	90
2	G4.17+36.67	237.6817	-4.0717	M15AI05	CV Daisy	0.55	13.8	130	87
3	G4.55+36.73	237.8058	-3.7993	M15AI05	CV Daisy	1.55	14.1	130	88
4	G4.80+37.02	237.7933	-3.4799	M15AI05	CV Daisy	4.53	13.7	130	88
5	G5.70+36.84	238.31	-3.0125	M16AL003	CV Daisy	0.01	15.9	120	83
6	G6.04+36.77	238.5362	-2.8793	M16AL003	CV Daisy	2.38	9.6	120	83
7	G27.31+37.33	246.8812	11.9261	M15AI57	Curvy Pong	2.73	13.7	190	128
8	G37.52+44.57	242.6992	21.7625	M15AI57	Curvy Pong	1.61	24.8	120	96
9	G45.12+61.11	225.65	29.3475	M13AC22	CV Daisy	1.03	13.0	180	170
10	G45.16-36.19	320.2862	-6.7184	M15AI57	Curvy Pong	0.64	15.9	370	-206
11	G48.63+34.42	256.0433	27.17	M15AI57	Curvy Pong	1.08	14.0	220	133
12	G48.88+30.61	260.2037	26.2654	M15AI57	Curvy Pong	0.57	10.2	240	134
13	G50.41-35.40	321.7487	-2.6816	M14AU02	CV Daisy	1.67	25.0	240	-131
14	G53.44-36.25	323.7992	-1.0448	M15AI29	CV Daisy	0.6	5.7	260	-143
15	G55.83-41.59	329.223	-2.5211	M19BP010	CV Daisy	2.3	21.3	170	-105
16	G63.65+47.67	241.9708	40.0444	M13AC22	CV Daisy	1.25	3.7	190	153
17	G92.49+42.88	242.3242	60.7558	M13AC22	CV Daisy	0.81	15.0	240	176
18	G93.60+55.86	221.0292	54.3658	M13AC22	CV Daisy	0.81	4.6	-	-
19	G96.05-50.34	355.8812	8.9585	M15AI57	Curvy Pong	0.79	20.1	170	-123
20	G105.07-38.06	357.7146	22.7272	M16AL003	CV Daisy	2.32	18.3	240	-141
21	G106.71-36.53	358.5827	24.566	M16AL003	CV Daisy	1.61	20.0	190	-105
22	G108.74-52.67	4.2204	9.2853	M15AI57	Curvy Pong	2.6	21.4	190	-144
23	G114.26-51.70	7.4162	10.7958	M15AI57	Curvy Pong	0.87	26.3	210	-151

Table A1 *continued*

Table A1 (*continued*)

No.	Field	RA	Dec.	Project ID	Scan Pattern ^a	Offset	rms	Distance	Altitude
		deg	deg			arcmin	mJy beam ⁻¹	pc	pc
(1)	(2)	(3)	(4)	(5)	(6)	(7)	(8)	(9)	(10)
24	G118.25-52.70	9.9721	10.0741	M15AI57	Curvy Pong	0.6	25.4	190	-144
25	G126.65-71.45	14.0508	-8.5967	M14AU02	CV Daisy	0.96	10.1	180	-164
26	G128.30-69.65	14.7304	-6.8572	M15AI57	Curvy Pong	0.48	13.4	160	-143
27	G128.76-69.46	14.9083	-6.6946	M15AI57	Curvy Pong	1.1	13.6	170	-152
28	G128.94-46.39	17.1279	16.3175	M16AL003	CV Daisy	3.56	32.1	190	-130
29	G132.04-45.20	19.5372	17.2079	M16AL003	CV Daisy	1.8	29.0	260	-174
30	G133.71-46.64	20.5246	15.6283	M19BP010	CV Daisy	2.17	25.8	180	-123
31	G135.11-49.44	21.0113	12.685	M19BP010	CV Daisy	4.59	24.2	230	-165
32	G138.36-69.45	18.2708	-7.2253	M15AI57	Curvy Pong	0.74	17.5	160	-143
33	G148.45+37.96	136.1146	65.9864	M19BP010	CV Daisy	3.05	20.5	330	210
34	G152.54-47.36	32.7862	10.8591	M14AU02	CV Daisy	0.96	8.8	180	-125
35	G157.44+30.33	117.2383	59.6949	M15AI29	CV Daisy	1.35	9.2	240	133
36	G158.51-33.99	43.7871	20.1953	M16AL003	CV Daisy	0.0	14.0	220	-112
37	G158.75-33.31	44.3617	20.6131	M16AL003	CV Daisy	2.54	17.8	230	-117
38	G158.86-34.19	43.9292	19.8755	M16AL003	CV Daisy	0.01	15.0	240	-127
39	G159.14-33.79	44.3671	20.0704	M16AL003	CV Daisy	0.0	14.8	220	-111
40	G159.21-34.28	44.1358	19.6369	M15BI061	CV Daisy	0.0	19.2	240	-128
41	G159.23-34.51	44.0096	19.4369	M15BI061	CV Daisy	0.0	19.2	240	-128
42	G159.41-34.37	44.1917	19.4608	M15BI061	CV Daisy	1.95	13.8	210	-106
43	G159.58-32.83	45.2717	20.6667	M16AL003	CV Daisy	0.39	17.7	210	-101
44	G159.66-34.31	44.4433	19.3998	MJLSY14B	CV Daisy	0.11	14.2	190	-99
45	G161.43-35.60	44.9392	17.5759	MJLSY14B	CV Daisy	4.28	14.2	180	-97
46	G161.67-35.92	44.8883	17.1405	M16AL003	CV Daisy	0.01	15.9	180	-97
47	G161.87-35.76	45.1096	17.1912	M14AU02	CV Daisy	1.02	15.4	160	-85
48	G174.35-39.98	50.0233	7.6149	M14AU02	CV Daisy	1.06	11.2	150	-89
49	G191.73-83.41	19.6517	-24.5784	M14AC02	CV Daisy	2.36	2.4	180	-172
50	G197.98+33.10	128.4412	26.1953	M14AU02	CV Daisy	0.44	17.2	260	151
51	G200.62+46.09	143.1058	27.3923	M14AC02	CV Daisy	0.37	3.8	-	-
52	G203.57-30.09	71.9871	-5.9299	M16AL003	CV Daisy	0.0	12.5	220	-99
53	G204.99+30.38	127.7183	19.6509	M13BU09	CV Daisy	1.48	2.4	240	133
54	G210.90-36.55	68.7596	-14.2279	M15BI041	CV Daisy	2.37	5.1	150	-77
55	G210.90+63.39	163.2525	24.9403	M15AI57	Curvy Pong	1.75	15.2	110	108
56	G211.62+32.23	131.6992	15.1041	M14AU02	CV Daisy	0.71	13.0	310	174
57	G220.55+60.12	161.2271	19.6588	M14AU02	CV Daisy	0.95	12.9	150	144
58	G228.99+30.91	137.2925	1.3597	M14AU15	CV Daisy	2.63	9.6	410	221
59	G235.60+38.28	146.4071	0.7633	M15AI57	Curvy Pong	1.9	16.7	180	123

Table A1 *continued*

Table A1 (*continued*)

No.	Field	RA	Dec.	Project ID	Scan Pattern ^a	Offset	rms	Distance	Altitude
(1)	(2)	deg	deg	(5)	(6)	arcmin	mJy beam ⁻¹	pc	pc
(1)	(2)	(3)	(4)	(5)	(6)	(7)	(8)	(9)	(10)
60	G235.67+38.00	146.2854	0.5485	M15AI57	Curvy Pong	2.83	16.7	180	123
61	G240.03+68.75	173.2117	16.1356	M15AI57	Curvy Pong	1.59	14.7	130	131
62	G251.29+73.32	179.3175	16.1378	M15AI57	Curvy Pong	1.41	15.3	120	127
63	G259.63+31.89	155.3671	-17.5	MJLSY01	Curvy Pong	32.99	38.8	240	139
64	G343.12+58.61	212.5196	2.0519	M14AU15	CV Daisy	2.32	9.3	140	127
65	G356.76+32.82	236.6396	-11.2159	M15AI57	Curvy Pong	1.88	29.4	150	89
66	G356.93+30.19	238.7129	-12.8761	M15AI57	Curvy Pong	0.98	28.8	180	102
67	G357.11+30.06	238.8917	-12.8652	M15AI57	Curvy Pong	0.7	26.7	160	92
68	G357.38+30.60	238.6437	-12.3195	M15AI57	Curvy Pong	0.51	25.0	150	84
69	G358.96+36.81	234.8908	-7.1984	M15AI57	Curvy Pong	1.73	27.5	130	88
70	G359.21+36.89	234.9154	-6.9746	M15AI57	Curvy Pong	1.4	14.2	120	83

NOTE—The serial number and the name of HLPC are listed in columns (1) and (2). The equatorial coordinates Right Ascension (RA) and Declination (Dec.) of the field center in Epoch J2000 are listed in columns (3) and (4). The project ID and scan pattern of the JCMT SCUBA-2 observation are listed in columns (5) and (6). The angular offset, which is defined by the angular distance from the field center to the center of the corresponding PGCC, is listed in column (7). The rms noise of the field is listed in column (8). The distance derived from dust map is listed in column (9). The altitude from the Galactic mid-plane is listed in column (10). This table is available in its entirety in machine-readable form.

^aCV Daisy = Constant Velocity Daisy; Curvy Pong = Rotating Curvy Pong.

^bThe rms noise within the “cut-off radius”.

B. SOURCE EXTRACTION

To avoid large marginal noise features masquerading as sources, we set a “cut-off radius” within which we estimate noise and extract sources for each field. The “cut-off radius” depends on FoV. For the CV Daisy observation mode, the radius is set to 5′. For Curvy Pong, the radius is set 10′. One exception is the field 63 with FoV ∼ 90′, so we set the diameter to be ∼ 67′. We carefully select emission-free pixels and take the root mean square (rms) as a uniform noise σ in each field (i.e., column (8) of Table A1). An intensity threshold of 3σ , a step of 2σ , and a minimum number of pixels (12 in our case) slightly larger than those contained in a JCMT beam are used for the input of the algorithm. In the output, “leaves” are the smallest structures and then defined as detected sources or sources hereafter.

Figure B1 displays all of the SCUBA-2 fields towards HLPCs. The “cut-off radius” utilized for source extraction is demarcated by the black dashed circles. The red contours demarcate the mask of extracted sources, while

the outcomes of the 2D Gaussian fitting are visualized through orange ellipses.

C. L183 PRESTELLAR CORES

Assuming that total emission F_{int} in column (6) of Table 1 is dust blackbody emission, then the mass of the three prestellar cores in L183 can be derived from,

$$M = \frac{F_{\text{int}} \mathcal{R} D^2}{\kappa_{\nu} B_{\nu}(T_{\text{dust}})}, \quad (\text{C1})$$

where D is distance of 120 pc and T_{dust} is estimated from the temperature map which is derived from pixelwise SED fitting by Karoly et al. (2020). As a result, $M_1 = 1.8 M_{\odot}$, $M_2 = 0.055 M_{\odot}$, and $M_3 = 0.19 M_{\odot}$. The mass of SMM1 is consistent with what has been derived in Karoly et al. (2020), but the masses of SMM2 and SMM3 are much smaller. The reason is likely the 6 times better sensitivity in Karoly et al. (2020) than ours, resulting in more extended emission being included.

The physical radius R can be derived from deconvolved size by $\eta \sqrt{\sigma_{\text{maj}} \sigma_{\text{min}}} \times D$ where $\eta = 2.4$ (Rosolowsky et al. 2010). We obtain $R_1 = 7000$ au, $R_2 = 2500$ au, and $R_3 = 3300$ au. And the averaged

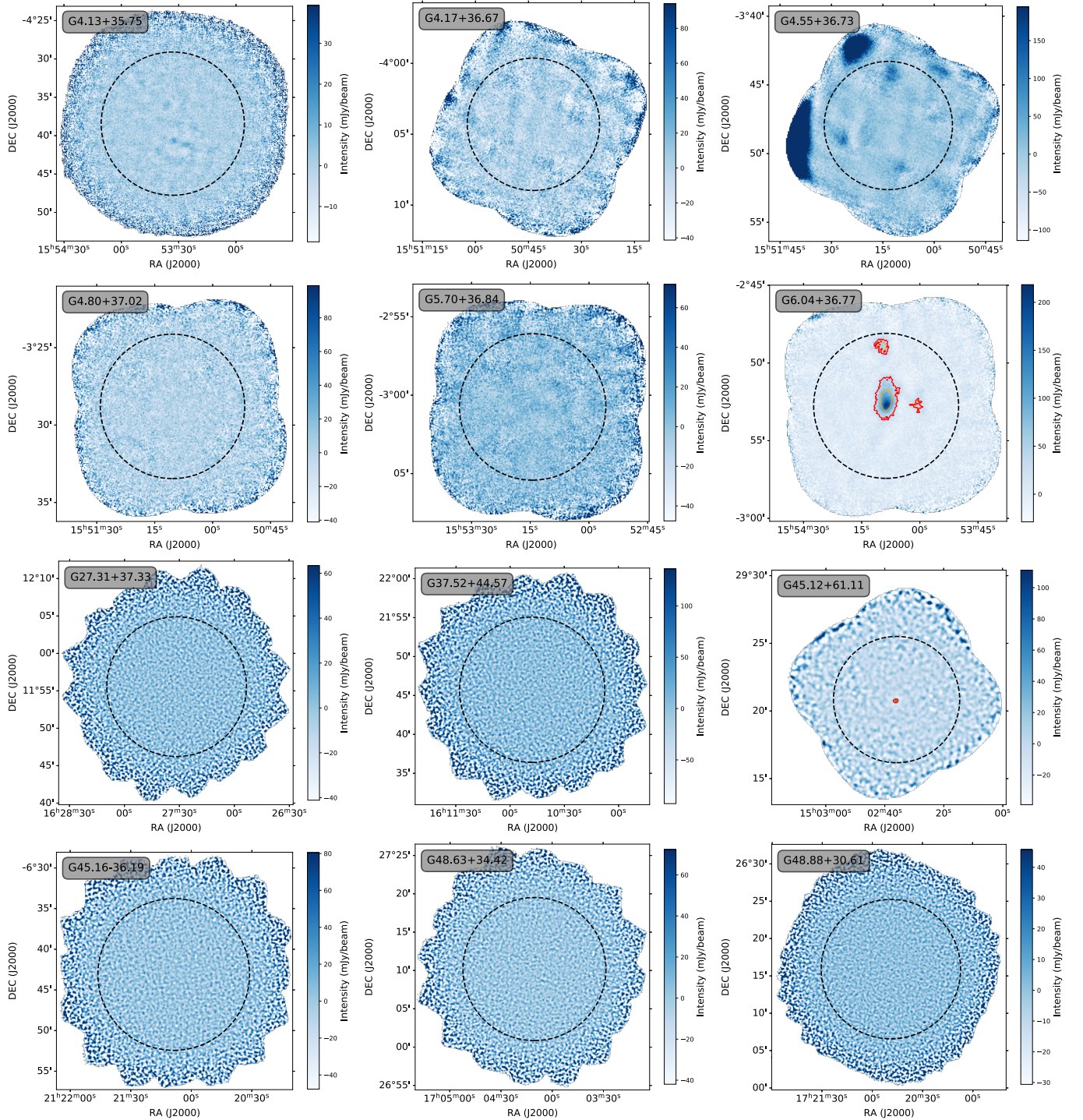


Figure B1. Full atlas for 70 HLPCs in SCUBA-2 observations. The “cut-off radius” utilized for source extraction is demarcated by the black dashed circles. The red contours demarcate the mask of extracted sources, while the outcomes of the 2D Gaussian fitting are visualized through orange ellipses. The complete figure set (6 images) will be available in the online journal.

volume density of molecular hydrogen can be calculated assuming a sphere as,

$$\bar{n}(\text{H}_2) = \frac{3M_i}{4\pi R_i^3 \mu_{\text{H}_2} m_{\text{H}}}, \quad i = 1, 2, 3. \quad (\text{C2})$$

So we derive $\bar{n}_1 = 1.7 \times 10^5 \text{ cm}^{-3}$, $\bar{n}_2 = 1.0 \times 10^5 \text{ cm}^{-3}$, and $\bar{n}_3 = 1.6 \times 10^5 \text{ cm}^{-3}$, which are all consistent with values in [Karoly et al. \(2020\)](#).

REFERENCES

- Astropy Collaboration, Robitaille, T. P., Tollerud, E. J., et al. 2013, *A&A*, 558, A33, doi: [10.1051/0004-6361/201322068](https://doi.org/10.1051/0004-6361/201322068)
- Astropy Collaboration, Price-Whelan, A. M., Sipőcz, B. M., et al. 2018, *AJ*, 156, 123, doi: [10.3847/1538-3881/aabc4f](https://doi.org/10.3847/1538-3881/aabc4f)
- Astropy Collaboration, Price-Whelan, A. M., Lim, P. L., et al. 2022, *ApJ*, 935, 167, doi: [10.3847/1538-4357/ac7c74](https://doi.org/10.3847/1538-4357/ac7c74)
- Beckwith, S. V. W., Sargent, A. I., Chini, R. S., & Guesten, R. 1990, *AJ*, 99, 924, doi: [10.1086/115385](https://doi.org/10.1086/115385)
- Benson, P. J., & Myers, P. C. 1983, *ApJ*, 270, 589, doi: [10.1086/161151](https://doi.org/10.1086/161151)
- . 1989, *ApJS*, 71, 89, doi: [10.1086/191365](https://doi.org/10.1086/191365)
- Berriman, G. B., & Good, J. C. 2017, *PASP*, 129, 058006, doi: [10.1088/1538-3873/aa5456](https://doi.org/10.1088/1538-3873/aa5456)
- Blitz, L., Magnani, L., & Mundy, L. 1984, *ApJL*, 282, L9, doi: [10.1086/184293](https://doi.org/10.1086/184293)
- Braine, J., Sun, Y., Shimajiri, Y., et al. 2023, *A&A*, 676, A27, doi: [10.1051/0004-6361/202039923](https://doi.org/10.1051/0004-6361/202039923)
- Cañameras, R., Nesvadba, N. P. H., Guery, D., et al. 2015, *A&A*, 581, A105, doi: [10.1051/0004-6361/201425128](https://doi.org/10.1051/0004-6361/201425128)
- Dame, T. M., Ungerechts, H., Cohen, R. S., et al. 1987, *ApJ*, 322, 706, doi: [10.1086/165766](https://doi.org/10.1086/165766)
- Dapp, W. B., & Basu, S. 2009, *MNRAS*, 395, 1092, doi: [10.1111/j.1365-2966.2009.14616.x](https://doi.org/10.1111/j.1365-2966.2009.14616.x)
- Dempsey, J. T., Friberg, P., Jenness, T., et al. 2013, *MNRAS*, 430, 2534, doi: [10.1093/mnras/stt090](https://doi.org/10.1093/mnras/stt090)
- Dickens, J. E., Irvine, W. M., Snell, R. L., et al. 2000, *ApJ*, 542, 870, doi: [10.1086/317040](https://doi.org/10.1086/317040)
- Eden, D. J., Liu, T., Kim, K.-T., et al. 2019, *MNRAS*, 485, 2895, doi: [10.1093/mnras/stz574](https://doi.org/10.1093/mnras/stz574)
- Evans, N. J., Kim, J.-G., & Ostriker, E. C. 2022, *ApJL*, 929, L18, doi: [10.3847/2041-8213/ac6427](https://doi.org/10.3847/2041-8213/ac6427)
- Franco, G. A. P. 1989, *A&A*, 223, 313
- Frye, B. L., Pascale, M., Qin, Y., et al. 2019, *ApJ*, 871, 51, doi: [10.3847/1538-4357/aaeff7](https://doi.org/10.3847/1538-4357/aaeff7)
- Gaia Collaboration, Prusti, T., de Bruijne, J. H. J., et al. 2016, *A&A*, 595, A1, doi: [10.1051/0004-6361/201629272](https://doi.org/10.1051/0004-6361/201629272)
- Green, G. M., Schlafly, E., Zucker, C., Speagle, J. S., & Finkbeiner, D. 2019, *ApJ*, 887, 93, doi: [10.3847/1538-4357/ab5362](https://doi.org/10.3847/1538-4357/ab5362)
- Green, G. M., Schlafly, E. F., Finkbeiner, D. P., et al. 2014, *ApJ*, 783, 114, doi: [10.1088/0004-637X/783/2/114](https://doi.org/10.1088/0004-637X/783/2/114)
- Griv, E., Gedalin, M., Pietrukowicz, P., Majaess, D., & Jiang, I.-G. 2021, *MNRAS*, 502, 4194, doi: [10.1093/mnras/stab321](https://doi.org/10.1093/mnras/stab321)
- Healey, S. E., Romani, R. W., Cotter, G., et al. 2008, *ApJS*, 175, 97, doi: [10.1086/523302](https://doi.org/10.1086/523302)
- Jacob, J. C., Katz, D. S., Berriman, G. B., et al. 2010, *Montage: An Astronomical Image Mosaicking Toolkit*, Astrophysics Source Code Library, record ascl:1010.036. <http://ascl.net/1010.036>
- Johnstone, D., Di Francesco, J., & Kirk, H. 2004, *ApJL*, 611, L45, doi: [10.1086/423737](https://doi.org/10.1086/423737)
- Juvela, M., Mattila, K., Lehtinen, K., et al. 2002, *A&A*, 382, 583, doi: [10.1051/0004-6361:20011539](https://doi.org/10.1051/0004-6361:20011539)
- Karoly, J., Soam, A., Andersson, B. G., et al. 2020, *ApJ*, 900, 181, doi: [10.3847/1538-4357/abad37](https://doi.org/10.3847/1538-4357/abad37)
- Kirk, J. M., Ward-Thompson, D., & André, P. 2005, *MNRAS*, 360, 1506, doi: [10.1111/j.1365-2966.2005.09145.x](https://doi.org/10.1111/j.1365-2966.2005.09145.x)
- Lee, C. W., & Myers, P. C. 1999, *ApJS*, 123, 233, doi: [10.1086/313234](https://doi.org/10.1086/313234)
- Lee, C. W., Myers, P. C., & Tafalla, M. 2001, *ApJS*, 136, 703, doi: [10.1086/322534](https://doi.org/10.1086/322534)
- Lin, Y., Spezzano, S., Pineda, J. E., et al. 2023, arXiv e-prints, arXiv:2308.12835, doi: [10.48550/arXiv.2308.12835](https://doi.org/10.48550/arXiv.2308.12835)
- Liu, T., Wu, Y., & Zhang, H. 2013, *ApJL*, 775, L2, doi: [10.1088/2041-8205/775/1/L2](https://doi.org/10.1088/2041-8205/775/1/L2)
- Liu, T., Kim, K.-T., Juvela, M., et al. 2018, *ApJS*, 234, 28, doi: [10.3847/1538-4365/aaa3dd](https://doi.org/10.3847/1538-4365/aaa3dd)
- Low, F. J., Beintema, D. A., Gautier, T. N., et al. 1984, *ApJL*, 278, L19, doi: [10.1086/184213](https://doi.org/10.1086/184213)
- MacKenzie, T. P., Scott, D., Bianconi, M., et al. 2017, *MNRAS*, 468, 4006, doi: [10.1093/mnras/stx512](https://doi.org/10.1093/mnras/stx512)
- Magnani, L., Blitz, L., & Mundy, L. 1985, *ApJ*, 295, 402, doi: [10.1086/163385](https://doi.org/10.1086/163385)
- Magnani, L., & de Vries, C. P. 1986, *A&A*, 168, 271
- Magnani, L., Hartmann, D., & Speck, B. G. 1996, *ApJS*, 106, 447, doi: [10.1086/192344](https://doi.org/10.1086/192344)
- Mairs, S., Johnstone, D., Kirk, H., et al. 2015, *MNRAS*, 454, 2557, doi: [10.1093/mnras/stv2192](https://doi.org/10.1093/mnras/stv2192)
- Malinen, J., Juvela, M., Zahorecz, S., et al. 2014, *A&A*, 563, A125, doi: [10.1051/0004-6361/201323026](https://doi.org/10.1051/0004-6361/201323026)
- Mann, H. B., & Whitney, D. R. 1947, *The Annals of Mathematical Statistics*, 18, 50, doi: [10.1214/aoms/1177730491](https://doi.org/10.1214/aoms/1177730491)
- McGehee, P. M. 2008, in *Handbook of Star Forming Regions*, Volume II, ed. B. Reipurth, Vol. 5, 813
- Meng, F., Wu, Y., & Liu, T. 2013, *ApJS*, 209, 37, doi: [10.1088/0067-0049/209/2/37](https://doi.org/10.1088/0067-0049/209/2/37)
- Miville-Deschênes, M.-A., & Lagache, G. 2005, *ApJS*, 157, 302, doi: [10.1086/427938](https://doi.org/10.1086/427938)
- Montillaud, J., Juvela, M., Rivera-Ingraham, A., et al. 2015, *A&A*, 584, A92, doi: [10.1051/0004-6361/201424063](https://doi.org/10.1051/0004-6361/201424063)
- Myers, P. C. 1983, *ApJ*, 270, 105, doi: [10.1086/161101](https://doi.org/10.1086/161101)

- Myers, P. C., & Benson, P. J. 1983, *ApJ*, 266, 309, doi: [10.1086/160780](https://doi.org/10.1086/160780)
- Myers, P. C., Linke, R. A., & Benson, P. J. 1983, *ApJ*, 264, 517, doi: [10.1086/160619](https://doi.org/10.1086/160619)
- Neugebauer, G., Habing, H. J., van Duinen, R., et al. 1984, *ApJL*, 278, L1, doi: [10.1086/184209](https://doi.org/10.1086/184209)
- Pagani, L., Lagache, G., Bacmann, A., et al. 2003, *A&A*, 406, L59, doi: [10.1051/0004-6361:20030903](https://doi.org/10.1051/0004-6361:20030903)
- Planck Collaboration, Ade, P. A. R., Aghanim, N., et al. 2011a, *A&A*, 536, A23, doi: [10.1051/0004-6361/201116472](https://doi.org/10.1051/0004-6361/201116472)
- . 2011b, *A&A*, 536, A7, doi: [10.1051/0004-6361/201116474](https://doi.org/10.1051/0004-6361/201116474)
- . 2014, *A&A*, 571, A29, doi: [10.1051/0004-6361/201321523](https://doi.org/10.1051/0004-6361/201321523)
- . 2016, *A&A*, 594, A28, doi: [10.1051/0004-6361/201525819](https://doi.org/10.1051/0004-6361/201525819)
- Plotkin, R. M., Anderson, S. F., Hall, P. B., et al. 2008, *AJ*, 135, 2453, doi: [10.1088/0004-6256/135/6/2453](https://doi.org/10.1088/0004-6256/135/6/2453)
- Reipurth, B., & Heathcote, S. 1990, *A&A*, 229, 527
- Rosolowsky, E., Dunham, M. K., Ginsburg, A., et al. 2010, *ApJS*, 188, 123, doi: [10.1088/0067-0049/188/1/123](https://doi.org/10.1088/0067-0049/188/1/123)
- Rosolowsky, E. W., Pineda, J. E., Kauffmann, J., & Goodman, A. A. 2008, *ApJ*, 679, 1338, doi: [10.1086/587685](https://doi.org/10.1086/587685)
- Samus', N. N., Kazarovets, E. V., Durlevich, O. V., Kireeva, N. N., & Pastukhova, E. N. 2017, *Astronomy Reports*, 61, 80, doi: [10.1134/S1063772917010085](https://doi.org/10.1134/S1063772917010085)
- Shu, F. H., Adams, F. C., & Lizano, S. 1987, *ARA&A*, 25, 23, doi: [10.1146/annurev.aa.25.090187.000323](https://doi.org/10.1146/annurev.aa.25.090187.000323)
- Swinbank, A. M., Smail, I., Longmore, S., et al. 2010, *Nature*, 464, 733, doi: [10.1038/nature08880](https://doi.org/10.1038/nature08880)
- Toth, L. V., Haikala, L. K., Liljestroem, T., & Mattila, K. 1995, *A&A*, 295, 755
- Truebenbach, A. E., & Darling, J. 2017, *MNRAS*, 468, 196, doi: [10.1093/mnras/stx456](https://doi.org/10.1093/mnras/stx456)
- Ward-Thompson, D., Motte, F., & Andre, P. 1999, *MNRAS*, 305, 143, doi: [10.1046/j.1365-8711.1999.02412.x](https://doi.org/10.1046/j.1365-8711.1999.02412.x)
- Ward-Thompson, D., Scott, P. F., Hills, R. E., & Andre, P. 1994, *MNRAS*, 268, 276, doi: [10.1093/mnras/268.1.276](https://doi.org/10.1093/mnras/268.1.276)
- Ward-Thompson, D., Pattle, K., Kirk, J. M., et al. 2016, *MNRAS*, 463, 1008, doi: [10.1093/mnras/stw1978](https://doi.org/10.1093/mnras/stw1978)
- Whitworth, A. P., & Ward-Thompson, D. 2001, *ApJ*, 547, 317, doi: [10.1086/318373](https://doi.org/10.1086/318373)
- Wright, E. L., Chen, X., Odegard, N., et al. 2009, *ApJS*, 180, 283, doi: [10.1088/0067-0049/180/2/283](https://doi.org/10.1088/0067-0049/180/2/283)
- Wu, Y., Liu, T., Meng, F., et al. 2012, *ApJ*, 756, 76, doi: [10.1088/0004-637X/756/1/76](https://doi.org/10.1088/0004-637X/756/1/76)
- Xu, F., Wu, Y., Liu, T., et al. 2021, *ApJ*, 920, 103, doi: [10.3847/1538-4357/ac1686](https://doi.org/10.3847/1538-4357/ac1686)
- Zucker, C., Goodman, A. A., Alves, J., et al. 2022, *Nature*, 601, 334, doi: [10.1038/s41586-021-04286-5](https://doi.org/10.1038/s41586-021-04286-5)